A static stability budget analysis reveals that horizontal and vertical advection both conall times throughout the upper troposphere and lower stratosphere. Advection is particularly important within the eye, where is acts to desta-bi-lize the layer near and above the cold-point tropopause. Out-side of the eye, a strong radial-vertical circulation develops during RI, without outflow below the tropopause and inflow above. Turbulence induced by strong vertical wind shear above and below the upper-tropospheric outflow maximum provides forcing for both stabilization and destabilization in the tropopause layer. Meanwhile, as organized convection reaches the tropopause, radiative heating tendencies at the top of the cirrus canopy act to desta-bi-lize the up-per tro-po-sphere and sta-bi-lize the lower strato-sphere. This com-bi-nation of turbulent mixing and radiative heating plays an important role in the devel-opment of the strong stable layer immediately above the cold-point tropopause.

The resuts suggest that turbulence and radiation both play fundamental roles in the upper-level static stability evolution of TCs. The conclusions are robust to changes in the initial thermodynamic profile and prescribed vertical mixing length within a reasonable range of values.

Tropopause Evolution in a Rapidly Intensifying Tropical Cyclone: A Static Stability Budget Analysis in an Idealized, Axisymmetric Framework

Patrick Duran* and John Molinari

University at Albany, State University of New York, Albany, NY

*Corresponding author address: Department of Atmospheric and Environmental Sciences, University at Albany, State University of New York, 1400 Washington Avenue, Albany, NY.
E-mail: pduran2008@gmail.com

ABSTRACT

1. Introduction

After undergoing a remarkably rapid intensification (RI), Hurricane Patricia (2015) set a new record as the strongest tropical cyclone (TC) ever observed in the Western Hemisphere (Kimberlain et al. 2016; Rogers et al. 2017). High-altitude dropsonde observations taken during the Tropical Cyclone Intensity (TCI) experiment captured this RI in unprecedented detail (Doyle et al. 2017). These observations revealed dramatic changes in the structure of the cold-point tropopause and upper-level static stability as the storm intensified (Duran and Molinari 2018).

At tropical storm intensity, shortly before RI commenced, a strong inversion layer existed just above Patricia's cold-point tropopause, which was located near 17.2 km. During the first half of the RI period, this inversion layer weakened throughout Patricia's inner core, with the weakening most pronounced over the developing eye. By the time the storm reached its maximum intensity, the inversion layer over the eye had disappeared almost completely, which was accompanied by an increase in the tropopause height to a level at or above the highest-available dropsonde data point (18.3 km) at two locations. Meanwhile over the eyewall region, the static stability re-strengthened and the tropopause was limited to a level at or below 17.5 km. The mechanisms that led to these changes in upper-level static stability and tropopause height are the subject of the current paper.

Despite the importance of tropopause-layer thermodynamics in theoretical models of hurricanes (Emanuel and Rotunno 2011; Emanuel 2012), few papers have examined the upper-tropospheric evolution of TCs. Komaromi and Doyle (2017) found that stronger TCs tended to have a higher and warmer tropopause over their inner core than weaker TCs. Their results are consistent with the evolution observed over the inner core of Hurricane Patricia, in which the tropopause height increased and the tropopause temperature warmed throughout RI (Duran and Molinari 2018).

Idealized simulations of a TC analyzed by Ohno and Satoh (2015) suggested that the development of an upper-level warm core near the TC storm center acted to decrease the static stability near the tropopause (see their Fig.). Although the mechanisms that drive this static stability evolution have not been examined explicitly, Stern and Zhang (2013) described the development of the TC warm core using a potential temperature (θ) budget analysis. They found that radial and vertical advection both played important roles in warm core development throughout RI, and subgrid-scale diffusion became particularly important during the later stage of RI. To our knowledge, the only paper that has examined explicitly the static stability evolution in a modeled TC is Kepert et al. (2016), but their analysis was limited to the boundary layer. The analysis herein is based upon that of Stern and Zhang (2013), except using a static stability budget similar to that of Kepert et al. (2016), with a focus on the upper troposphere and lower stratosphere.

2. Model Setup

The numerical simulations were performed using version 19.4 of Cloud Model 1 (CM1) described in Bryan and Rotunno (2009). The equations of motion were integrated on a 3000-km-wide, 30-km-deep axisymmetric grid with 1-km horizontal and 250-m vertical grid spacing. The computations were performed on an f-plane at 15°N latitude, over a sea surface with constant temperature of 30.5°C, which matches that observed near Hurricane Patricia (2015; Kimberlain et al. 2016). Horizontal turbulence was parameterized using the Smagorinsky scheme described in Bryan and Rotunno (2009, pg. 1773), with a prescribed mixing length that varied linearly from 100 m at a surface pressure of 1015 hPa to 1000 m at a surface pressure of 900 hPa. This formulation allows for realistically-large horizontal mixing lengths near the hurricane's inner core, consistent with the results of Bryan (2012), while not over-representing horizontal turbulence in convection at outer radii. Vertical turbulence was parameterized using the formulation of Markowski and

Bryan (2016, their Eq. 6), using an asymptotic vertical mixing length of 100 m. A Rayleigh damping layer was applied outside of the 2900-km radius and above the 25-km level to prevent spurious gravity wave reflection at the model boundaries. Microphysical processes were parameterized using the Thompson et al. (2004) microphysics scheme and radiative heating tendencies were computed every two minutes using the Rapid Radiative Transfer Model for GCMs (RRTMG) longwave and shortwave schemes (Iacono et al. 2008). The initial temperature and humidity field was horizontally homogeneous and determined by averaging all Climate Forecast System Reanalysis (CFSR) grid points within 100 km of Patricia's center of circulation at 18 UTC 21 October 2015. The vortex described in Rotunno and Emanuel (1987, their Eq. 37) was used to initialize the wind field, setting all parameters equal to the values used therein.

Although hurricanes simulated in an axisymmetric framework tend to be more intense than those observed in nature, the intensity evolution of this simulation matches reasonably well with that observed in Hurricane Patricia. After an initial spin-up period of about 20 hours, the modeled storm (Fig.1, blue lines) began an RI period that lasted approximately 30 hours. After this RI, the storm continued to intensify more slowly until the maximum 10-m wind speed reached 89 m s^{-1} and the minimum sea-level pressure reached its minimum of 846 mb, 81 hours into the simulation. Hurricane Patricia (red stars) exhibited a similar intensity evolution, with an RI period leading to a maximum 10-m wind speed of 95 m s^{-1} and a minimum sea-level pressure of 872 hPa. Despite the limitations of the axisymmetric framework, the extraordinary intensity of Hurricane Patricia and the rapidity of its intensification makes Patricia a particularly good candidate for axisymmetric analysis.

3. Budget Computation

The static stability can be expressed as the squared Brunt Väisälä frequency:

$$N_m^2 = \frac{g}{T}\left(\frac{\partial T}{\partial z} + \Gamma_m\right)\left(1 + \frac{T}{R_d/R_v + q_s}\frac{\partial q_s}{\partial T}\right) - \frac{g}{1+q_t}\frac{\partial q_t}{\partial z}, \tag{1}$$

where g is gravitational acceleration, T is temperature, R_d and R_v are the gas constants of dry air and water vapor, respectively, q_s is the saturation mixing ratio, q_t is the total condensate mixing ratio, and Γ_m is the moist-adiabatic lapse rate:

$$\Gamma_m = g(1+q_t)\left(\frac{1 + L_v q_s/R_d T}{c_{pm} + L_v \partial q_s/\partial T}\right), \tag{2}$$

where L_v is the latent heat of vaporization and c_{pm} is the specific heat of moist air at constant pressure. In the tropopause layer, q_s, $\partial q_s/\partial T$, and $\partial q_t/\partial z$ approach zero. In this limiting case, Eq. 1 reduces to:

$$N^2 = \frac{g}{\theta}\frac{\partial \theta}{\partial z}, \tag{3}$$

where θ is the potential temperature.

To compute N^2, CM1 uses Eq.1 in saturated environments and Eq. 3 in sub-saturated environments. For simplicity, however, only Eq. 3 will be employed for the budget computations herein[1].

Taking the time derivative of Eq. 3 yields the static stability tendency:

$$\frac{\partial N^2}{\partial t} = \frac{g}{\theta}\frac{\partial}{\partial z}\frac{\partial \theta}{\partial t} - \frac{g}{\theta^2}\frac{\partial \theta}{\partial z}\frac{\partial \theta}{\partial t}, \tag{4}$$

where the potential temperature tendency, $\partial\theta/\partial t$, can be written:

$$\frac{\partial \theta}{\partial t} = HADV + VADV + HTURB + VTURB + MP + RAD + DISS \tag{5}$$

Each term on the right-hand side of Eq. 5 represents a θ budget variable, each of which is output directly by the model every minute. HADV and VADV are the radial and vertical advective

[1]The validity of this approximation will be substantiated later in this section.

tendencies[2], HTURB and VTURB are the radial and vertical tendencies from the turbulence parameterization, MP is the tendency from the microphysics scheme, RAD is the tendency from the radiation scheme, and DISS is the tendency due to turbulent dissipation. This equation neglects Rayleigh damping, since this term is zero everywhere below 25 km, and the analysis domain does not extend to that level. Each term in Eq. 5 is substituted for $\partial\theta/\partial t$ in Eq. 4, yielding the contribution of each budget term to the static stability tendency. These terms are summed, yielding an instantaneous "budget change" in N^2 every minute. The budget changes are then averaged over 24-hour periods and compared to the total model change in N^2 over that same time period, i.e.:

$$\Delta N^2_{budget} = \frac{1}{\delta t}\sum_{t=t_0}^{t_0+\delta t} \left.\frac{\partial N^2}{\partial t}\right|_t \tag{6}$$

$$\Delta N^2_{model} = N^2_{t_0+\delta t} - N^2_{t_0} \tag{7}$$

$$Residual = \Delta N^2_{model} - \Delta N^2_{budget} \tag{8}$$

where t_0 is an initial time and δt is 24 hours.

Eqs. 6-8 are plotted for four consecutive 24-hour periods in Fig. 2. For this and all subsequent radial-vertical cross sections, a 1-2-1 smoother is applied once in the radial direction to eliminate $2\Delta r$ noise that appears in some of the raw model output and calculated fields. The left column of Fig. 2 depicts the model changes (Eq. 7), the center column depicts the budget changes (Eq. 6), and the right column depicts the residuals (Eq. 8). In every 24-hour period, the budget changes are nearly identical to the model changes, which is reflected in the near-zero residuals in the right column. This indicates that the budget accurately represents the model variability, which implies that the neglect of moisture in the budget computation introduces negligible error within the anaysis domain[3].

---

[2]These terms include the tendencies due to the diffusion that is implicit in the fifth-order advection scheme.

[3]This is not the case in the lower- and mid-troposphere, where the residual actually exceeds the budget variability in many places, likely due to the neglect of moisture; thus we limit this analysis to the upper troposphere and lower stratosphere.

In the tropopause layer, some of the budget terms are small enough to be ignored. To determine which of the budget terms are most important, a time series of the contribution of each of the budget terms in Eq. 5 to the tropopause-layer static stability tendency is plotted in Fig. 4. For this figure, each of the budget terms is computed using the method described in Section 3, except with 1-hour averaging intervals instead of 24-hour intervals. The absolute values of these tendencies are then averaged over a radius-height domain surrounding the tropopause and plotted as a time series[4]. Advection (Fig. 4, red line) plays an important role in the mean tropopause-layer static stability tendency at all times, and vertical turbulence (Fig. 4, blue line) and radiation (Fig. 4, dark green line) also contribute significantly. Although the contribution from horizontal turbulence (Fig. 4, purple line) becomes more important after 48 hours, it is confined to a very small region immediately surrounding the eyewall tangential velocity maximum (not shown), and is negligible throughout the rest of the tropopause layer. The remaining two processes - microphysics and dissipative heating (Fig. 4, orange and light green lines, respectively) - lie atop one another near zero. These time series indicate that, at all times, three budget terms dominate the tropopause-layer static stability tendency: advection, vertical turbulence, and radiation. Variations in the magnitude and spatial structure of these terms drive the static stability changes depicted in Fig. 2; subsequent sections will focus on these variations and what causes them.

[4]It will be seeen in subsequent figures that each of the terms contributes both positively and negatively to the N^2 tendency within the analysis domain. Thus, taking an average over the domain tends to wash out the positive and negative contributions. To circumvent this problem, the absolute value of each of the terms is averaged.

4. Results

a. Static stability evolution

The average N^2 over the first day of the simulation (Fig. 3a) indicates the presence of a weak static stability maximum just above the cold-point tropopause. Over the subsequent 24 hours, during the RI period, the static stability within and above this layer decreased near the storm center (Fig. 3b). This decreasing N^2 corresponded to an increase in the tropopause height within the developing eye, maximized at the storm center. Outside of the eye, meanwhile, the tropopause height decresed over the eyewall region (25-60-km radius) and increased only slightly outside of the 60-km radius. In this outer region, the N^2 maximum just above the tropopause strengthened during RI. These trends continued as the storm's intensity leveled off in the 48-72-hour period (Fig. 3c). The tropopause height increased to nearly 21 km at the storm center and sloped sharply downward to 16.3 km on the inner edge of the eyewall, near the 30 km radius. Static stability outside of the eye, meanwhile, continued to increase just above the cold-point tropopause. This N^2 evolution closely follows that observed in Hurricane Patricia (2015; Duran and Molinari 2018). The mechanisms that led to these static stability changes will be investigated in the subsequent sections.

b. Static stability budget analysis

(i) 0-24 hours The weakening of the lower-stratospheric static stability maximum during the initial spin-up period is reflected in the total N^2 budget change over this time (Fig. 5a). The 17-18-km layer was characterized by decreasing N^2 (purple shading), maximizing at the storm center. The layer immediately below the tropopause, meanwhile, saw strengthening N^2 during this time period. Although these tendencies extended out to the 200-km radius, they were particularly

pronounced at innermost radii. A comparison of the contributions of advection (Fig. 5b), vertical turbulence (Fig. 5c), and radiation (Fig. 5d) reveals that advection is primarily responsible for the change in static stability during this period. Although vertical turbulence acts in opposition to advection (i.e. it acts to stabilize regions that advection acts to destabilize), the magnitude of the advective tendencies is larger, particularly at the innermost radii. The sum of advection and vertical turbulence (Fig. 5e) almost exactly replicates the static stability tendencies above 17 km. Radiative tendencies (Fig. 5d) act to destabilize the layer below about 16 km and stabilize the layer between 16 and 17 km. The sum of advection, vertical turbulence, and radiation (Fig. 5f) reproduces the total change in N^2 almost exactly.

...Explain this in the context of radial and vertical velocities... ...See Stern and Zhang, Page 84, Section 3d... ...Add mention of total condensate and radiative heating tendencies as it relates to statbility tendency due to rad...

(ii) 24-48 hours During the RI period, N^2 within the eye generally decreased above 16 km and increased below (Fig. 6a). These tendencies at the innermost radii were driven almost entirely by advection (Fig. 6b); vertical turbulence (Fig. 6c) and radiation (Fig. 6d) contributed negligibly to the static stability tendencies in this region.

Outside of the eye, the N^2 evolution exhibited alternating layers of positive and negative tendencies. Near and above 18 km existed an upward-sloping region of decreasing N^2 that extended out to the 180-km radius. In this region, neither vertical turbulence nor radiation exhibited negative N^2 tendencies; advection was the only forcing for destabilization. Immediately below this layer was a region of increasing N^2, which sloped upward from 17 km near the 30-km radius to just below 18 km outside of the 100-km radius. Advection and vertical turbulence both contributed to this positive N^2 tendency, with advection playing an important role below about 17.5 km and and turbulence playing an important role above. The sum of advection and turbulence (Fig. 6e) reveals two discontiguous regions of increasing N^2 in the 17-18-km layer rather than one contiguous region. The addition of radiation to these two terms, however, (Fig. 6f) provides the link between these two regions, indicating that radiation also plays a role in strengthening the stable layer just above the tropopause. In the 16-17-km layer, a horizontally-extensive layer of decreasing N^2 also was forced by a combination of advection, vertical turbulence, and radiation. The sum of advection and vertical turbulence accounts for only a portion of the decreasing N^2 in this layer, and actually indicates forcing for stabilization near the 50-km radius and outside of the 130-km radius. Radiative tendencies overcome this forcing for stabilization in both of these regions to produce the radially-extensive region of destabilization observed just below the tropopause.

TWO REGIONS WHERE Panel (f) differs from panel (a): 30-60 km radial band below 16 km, which is actually canceled out by a vertical gradient of latent heating, and the thin region of strong stabilization between 15-17.5 km near r=30 km, which is canceled out by horizontal turbulence.

(iii) 48-72 hours After the storm's maximum wind speed leveled off near 80 m s^{-1}, the magnitude of the static stability tendencies within the eye decreased to near zero (Fig. 7a).

Outside of the eye, however, N^2 continued to increase just above the tropopause and decrease just below. The sum of advection and vertical turbulence (Fig. 7e) indicates that the increase of N^2 observed in the 17-18-km layer and inside of the 80-km radius cannot be attributed to these processes, since the sum of these two terms provided forcing for destabilization. Instead, radiation (Fig. 7d), provided the forcing for stabilization in this region. Outside of the 80-km radius, both advection (Fig. 7b) and vertical turbulence (Fig. 7c) provided forcing for stabilization near the 18-km level. The sum of the two terms indicates increasing N^2 near the 18-km level everywhere outside of the 80-km radius, but this stabilization is slightly weaker in the 90-120-km radial band than the observed value. The addition of radiation (Fig. 7f) provides the extra forcing for stabilization required to account for the observed increase in N^2. Outside of the 120-km radius, the region of radiative forcing for stabilization slopes downward, and the increase in N^2 observed near 18 km can be explained entirely by a combination of advection and vertical turbulence. The layer of decreasing $N^{@}$ observed near 17 km was forced primarily by vertical turbulence and radiation. Within most of this region, advection provided strong forcing for stabilization, but this forcing was outweighed by the negative N^2 tendencies induced by a combination of vertical turbulence and radiation.

5. Discussion

a. The role of advection

Advection played an important role in the tropopause-layer N^2 evolution at all stages of intensification, but for brevity, this section will focus only on the RI period. To investigate the advective processes more closely, the individual contributions of horizontal and vertical advection during the RI period are shown in Fig. 8, along with the corresponding time-mean radial and vertical velocities and θ. The N^2 tendencies due to the two advective components (Fig. 8a,b) exhibit strong cancellation, consistent with flow that is nearly isentropic. There are, however, some regions in which flow crosses θ surfaces; this flow accounts for all non-zero N^2 tendencies due to advection previously seen in Fig. 6b.

Some insight can be gained by considering the time tendency of the vertical θ gradient due to advection:

$$\left(\frac{\partial}{\partial t}\frac{\partial \theta}{\partial z}\right)_{adv} = -u\frac{\partial}{\partial r}\frac{\partial \theta}{\partial z} - w\frac{\partial}{\partial z}\frac{\partial \theta}{\partial z} - \frac{\partial u}{\partial z}\frac{\partial \theta}{\partial r} - \frac{\partial w}{\partial z}\frac{\partial \theta}{\partial z}. \tag{9}$$

The first two terms on the right-hand side of Eq. 9 represent advection of static stability by the radial and vertical wind, respectively. The third and fourth terms represent, respectively, the tilting of isentropes in the presence of vertical wind shear, and the spreading or compaction of isentropes through divergence of the vertical wind.

During the RI period, strong radial and vertical circulations developed near the tropopause, which forced high-magnitude N^2 tendencies due to advection (Fig. 8a,b). A layer of strong outflow developed at and below the tropopause during this period, with the outflow maximum (dashed cyan line) curving from the 14-km level at the 50-km radius to just below the 16-km level outside of the 80-km radius (Fig. 8c). The cyan line, by definition, represents the level at which the vertial gradient of radial velocity switched signs, with $\partial u/\partial z > 0$ below the line and $\partial u/\partial z < 0$ above. Notably, the N^2 tendency due to horizontal advection (Fig. 8a) also tended to switch signs very near this line, with stabilization below the outflow maximum and destabilization above. This suggests that vertical wind shear above and below the outflow maximum played an important role in the N^2 tendency during this time. Examination of the third term on the right-hand side of Eq. 9 reveals that tilting of isentropes within these shear layers contributed to the strong N^2 tendencies that flanked the outflow maximum. Outside of the eye and eyewall, isentropes generally sloped upward with radius, which means that θ decreased outward ($\partial\theta/\partial r < 0$). Thus, wherever $\partial u/\partial z > 0$, the tilting term forced an increase in N^2, and wherever $\partial u/\partial z < 0$, the tilting term forced a decrease in N^2. This is precisely the structure seen in Fig. 8a, which suggests that the tilting term

Meanwhile in the lower stratosphere, a thin layer of 2-4 m s^{-1} inflow developed a few hundred meters above the tropopause.

Radiative heating and turbulence viscosity figures?

Discuss how turbulence increases the static stability in some regions –¿ vertical gradients of turblence intensity.

Diurnal variability of of static stability in the upper troposphere is an interesting area of future research.

Acknowledgments. We are indebted to George Bryan for his continued development and support of Cloud Model 1. We also thank Jeffrey Kepert, Robert Fovell, and Erika Navarro for helpful conversations related to this work. ADD GRANT NUMBER

APPENDIX

Sensitivity experiments

The simulations exhibited some sentivity to the initial thermodynamic profile and the prescribed vertical mixing length. Although the details of the intensification and the tropopause-layer N^2 evolution varied when these quantities were changed, the conclusions of the paper remain unchanged.

a. Sensitivity to the initial thermodynamic profile

A number of sensitivity experiments were conducted using a variety of initial soundings. Changing the initial temperature and humidity profiles affected the timing of the onset of organized deep convection and the rapidity of intensification. In all simulations, however, convection eventually penetrated to the tropopause, at which time vertical turbulence and radiation combined with advection to adjust the N^2 profile toward that which was observed in the control run. By the end of the RI period in every simulation, all three proesses were actively modifying the N^2 profile near the tropopause.

b. Sensitivity to the vertical mixing length

The intensity of parameterized turbulence is highly dependent on a prescribed length scale. Since there is no theoretical or observational guidance for the selection of this mixing length, the value used in the control run (100 m) is based on the sensitivity experiments of Bryan (2012). Since the vertical eddy viscosity varies linearly with the vertical mixing length, prescribing a smaller mixing length produces smaller θ tendencies due to turbulence. Even with a mixing length on the low end of those tested by Bryan (2012), however, turbulence still plays a role in the tropopause-layer N^2 evolution. FIG shows the N^2 evolution in a simulation identical to the control run, except with a vertical mixing length of 50 m rather than 100 m. DESCRIPTION OF THE FIGURE

References

Bryan, G. H., 2012: Effects of surface exchange coefficients and turbulence length scales on the intensity and structure of numerically simulated hurricanes. *Mon. Wea. Rev.*, **140**, 1125–1143.

Bryan, G. H., and R. Rotunno, 2009: The maximum intensity of tropical cyclones in axisymmetric numerical model simulations. *Mon. Wea. Rev.*, **137**, 1770–1789.

Doyle, J. D., and Coauthors, 2017: A view of tropical cyclones from above: The Tropical Cyclone Intensity (TCI) Experiment. *Bull. Amer. Meteor. Soc.*, **98**, 2113–2134.

Duran, P., and J. Molinari, 2018: Dramatic inner-core tropopause variability during the rapid intensification of Hurricane Patricia (2015). *Mon. Wea. Rev.*, **XXX**, XXX–XXX.

Emanuel, K., 2012: Self-stratification of tropical cyclone outflow. Part II: Implications for storm intensification. *J. Atmos. Sci.*, **69**, 988–996.

Emanuel, K., and R. Rotunno, 2011: Self-stratification of tropical cyclone outflow. Part I: Implications for storm structure. *J. Atmos. Sci.*, **68**, 2236–2249.

Iacono, M. J., J. S. Delamere, E. J. Mlawer, M. W. Shephard, S. A. Clough, and W. D. Collins, 2008: Radiative forcing by long-lived greenhouse gases: Calculations with the AER radiative transfer models. *J. Geophys. Res.*, **113 (D13103)**.

Kepert, J. D., J. Schwendike, and H. Ramsay, 2016: Why is the tropical cyclone boundary layer not "well mixed"? *J. Atmos. Sci.*, **73**, 957–973.

Kimberlain, T. B., E. S. Blake, and J. P. Cangialosi, 2016: Tropical cyclone report: Hurricane Patricia. National Hurricane Center. [Available online at www.nhc.noaa.gov].

Komaromi, W. A., and J. D. Doyle, 2017: Tropical cyclone outflow and warm core structure as revealed by HS3 dropsonde data. *Mon. Wea. Rev.*, **145**, 1339–1359.

Markowski, P. M., and G. H. Bryan, 2016: LES of laminar flow in the PBL: A potential problem for convective storm simulations. *Mon. Wea. Rev.*, **144**, 1841–1850.

Ohno, T., and M. Satoh, 2015: On the warm core of a tropical cyclone formed near the tropopause. *J. Atmos. Sci.*, **72**, 551–571.

Rogers, R. F., S. Aberson, M. M. Bell, D. J. Cecil, J. D. Doyle, J. Morgerman, L. K. Shay, and C. Velden, 2017: Re-writing the tropical record books: The extraordinary intensification of Hurricane Patricia (2015). *Bull. Amer. Meteor. Soc.*, **98**, 2091–2112.

Rotunno, R., and K. A. Emanuel, 1987: An air-sea interaction theory for tropical cyclones. Part II: Evolutionary study using a nonhydrostatic axisymmetric numerical model. *J. Atmos. Sci.*, **44**, 542–561.

Stern, D. P., and F. Zhang, 2013: How does the eye warm? Part I: A potential temperature budget analysis of an idealized tropical cyclone. *J. Atmos. Sci.*, **70**, 73–89.

Thompson, G., R. M. Rasmussen, and K. Manning, 2004: Explicit forecasts of winter precipitation using an improved bulk microphysics scheme. Part I: Description and sensitivity analysis. *Mon. Wea. Rev.*, **132**, 519–542.

LIST OF FIGURES

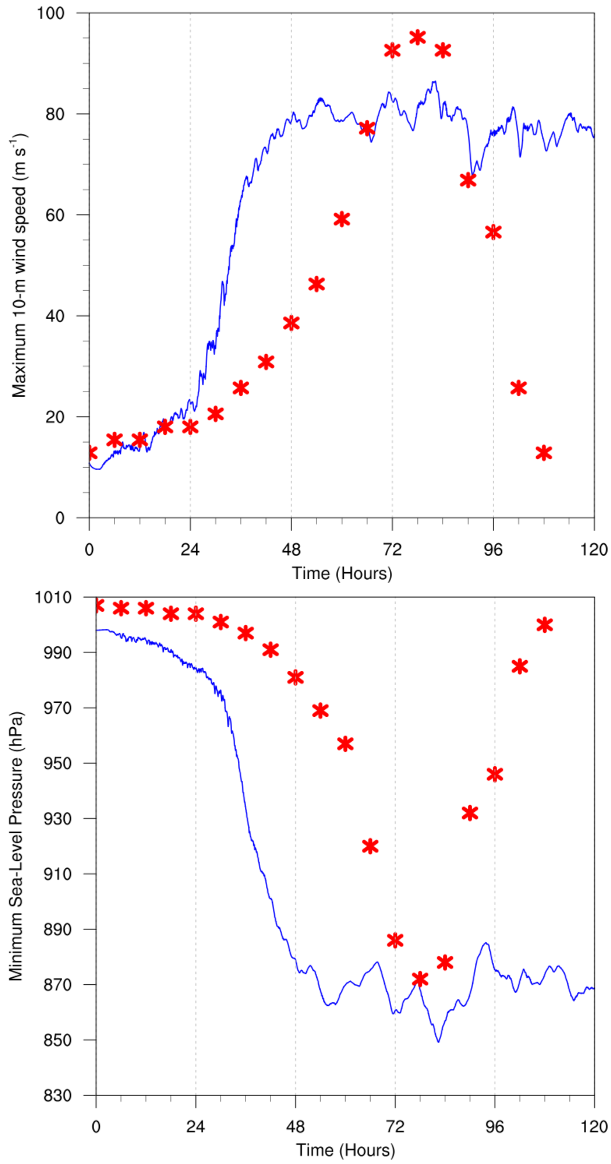

FIG. 1. The maximum 10-m wind speed (top panel; m s^{-1}) and minimum sea-level pressure (bottom panel; hPa) in the simulated storm (blue lines) and from Hurricane Patricia's best track (red stars).

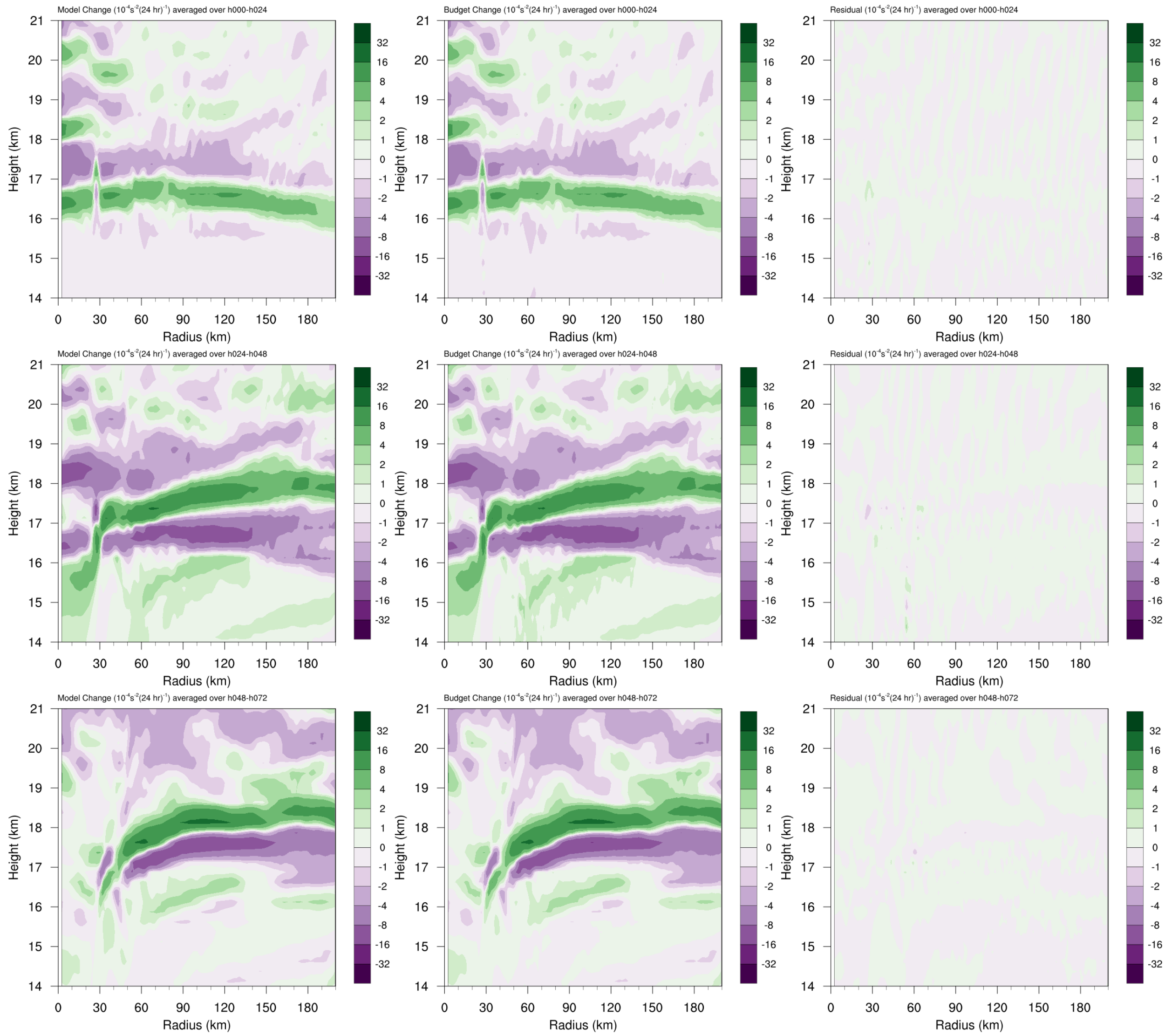

FIG. 2. Left panels: Twenty-four-hour changes in squared Brunt-Väisälä frequency (N^2; 10^{-4} s^{-2}) over (a) 0-24 hours, (b) 24-48 hours, (c) 48-72 hours. Middle Panels: The N^2 change over the same time periods computed using Eqs. 4-6, Right Panels: The budget residual over the same time periods, computed by subtracting the budget change (middle column) from the model change (left column).

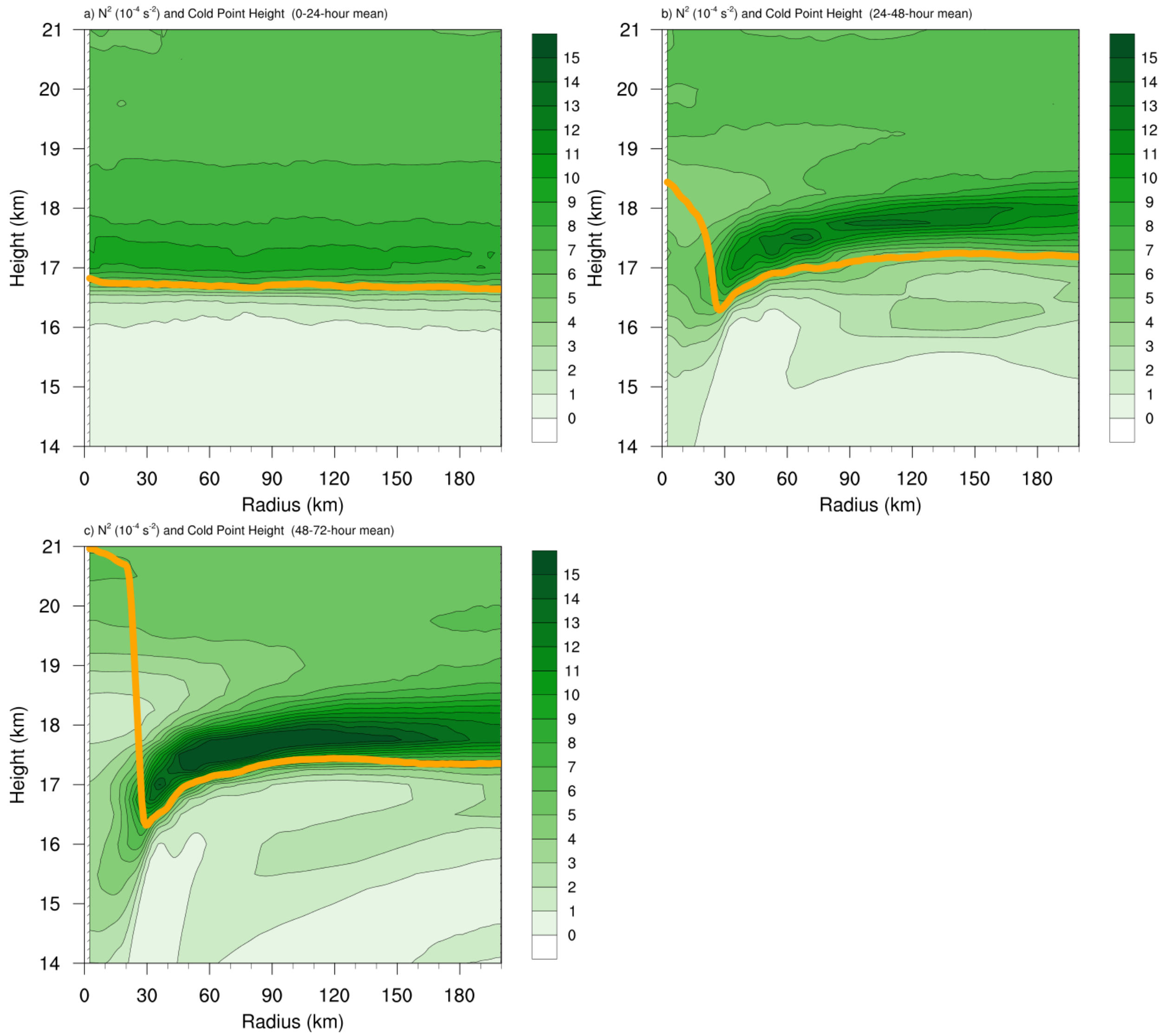

FIG. 3. Twenty-four-hour averages of squared Brunt-Väisälä frequency (N^2; 10^{-4} s^{-2}) over (a) 0-24 hours, (b) 24-48 hours, (c) 48-72 hours. Orange lines represent the cold-point tropopause averaged over the same time periods.

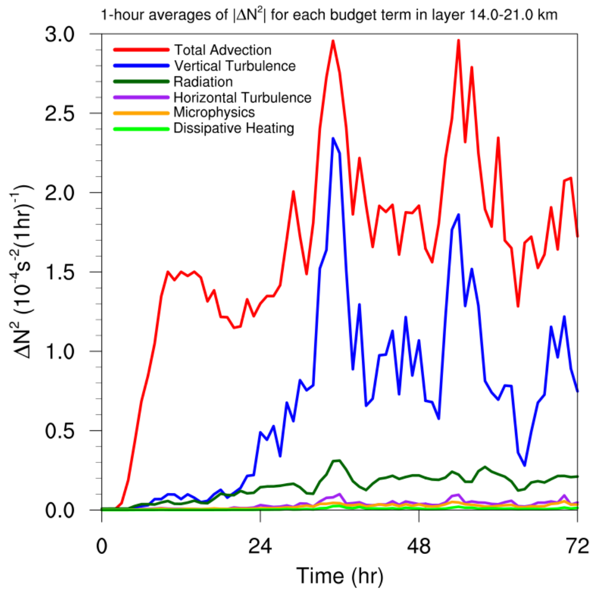

FIG. 4. Time series of the contribution of each of the budget terms to the time tendency of the squared Brunt-Väisälä frequency (N^2; 10^{-4} s^{-2}). For each budget term, the absolute value of the N^2 tendency is averaged temporally over 1-hour periods (using output every minute), and spatially in a region extending from 0 to 200 km radius and 14 to 21 km altitude.

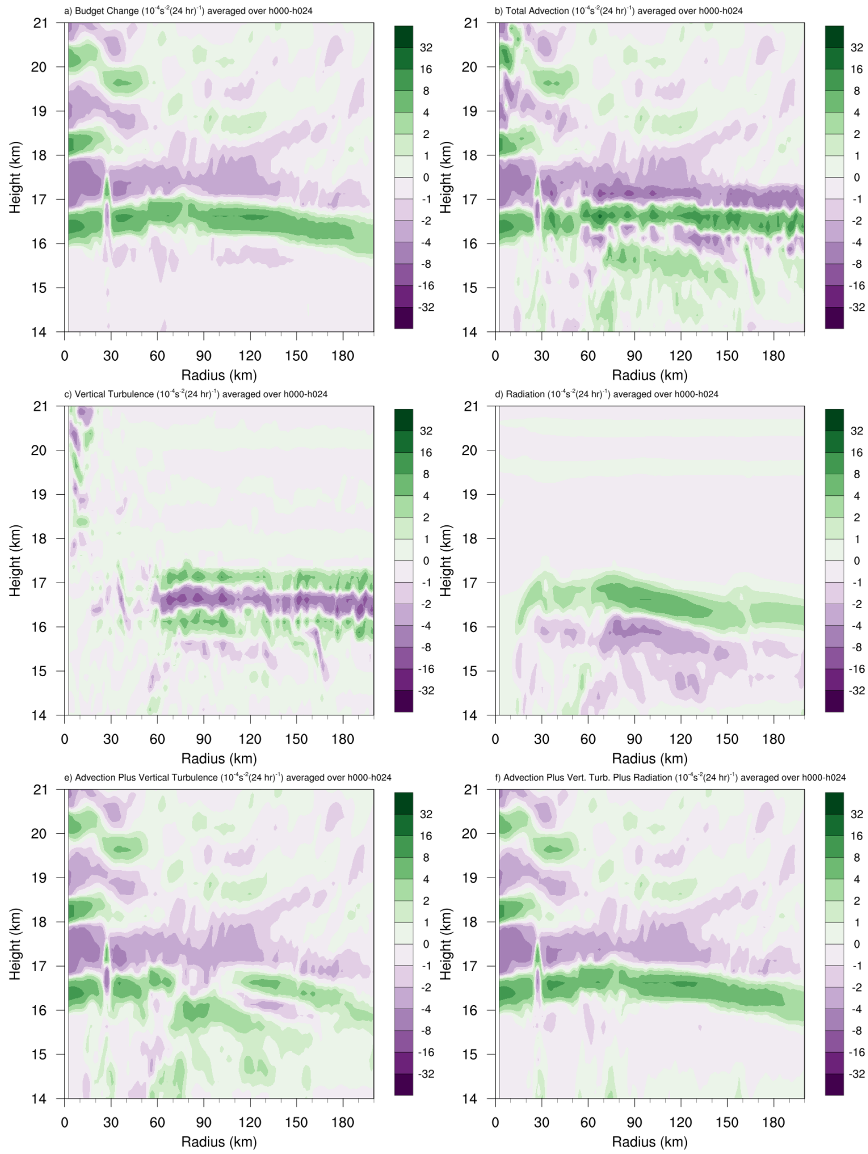

FIG. 5. (a) Total change in N^2 over the 0-24-hour period (10^{-4} s^{-2} $(24\ hr)^{-1}$) and the contributions to that change from (b) the sum of horizontal and vertical advection, (c) vertical turbulence, (d) longwave and shortwave radiation, (e) the sum of horizontal advection, vertical advection, and vertical turublence, and (f) the sum of horizontal advection, vertical advection, vertical turbulence, and longwave and shortwave radiation.

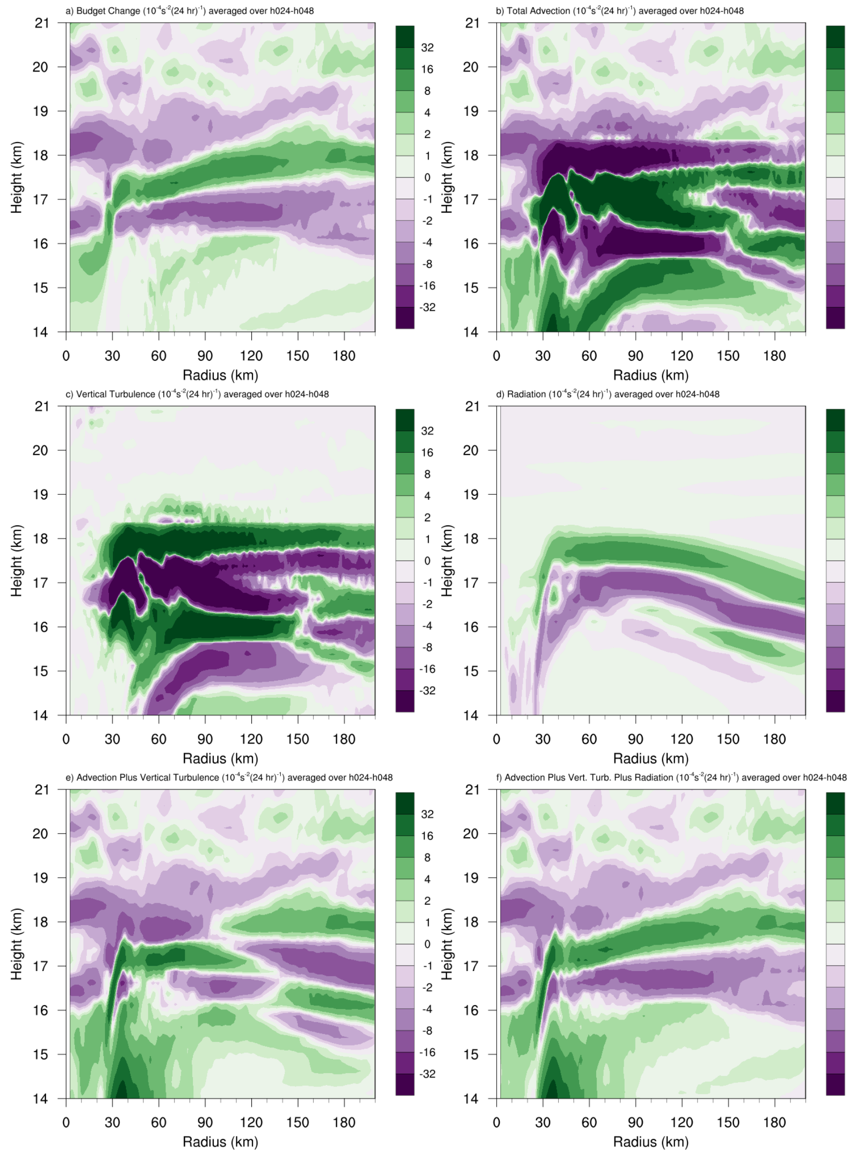

FIG. 6. As in Fig. 5, but for the 24-48-hour period.

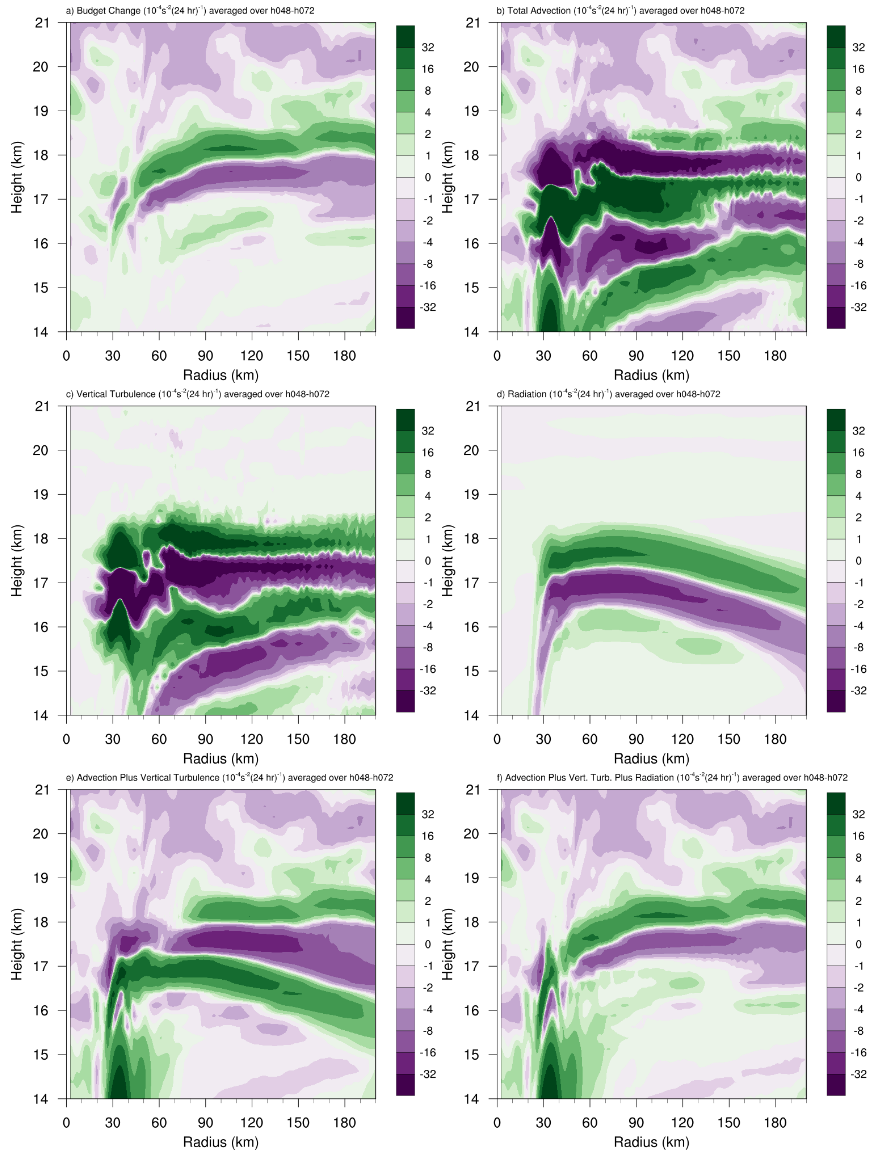

FIG. 7. As in Fig. 5, but for the 48-72-hour period.

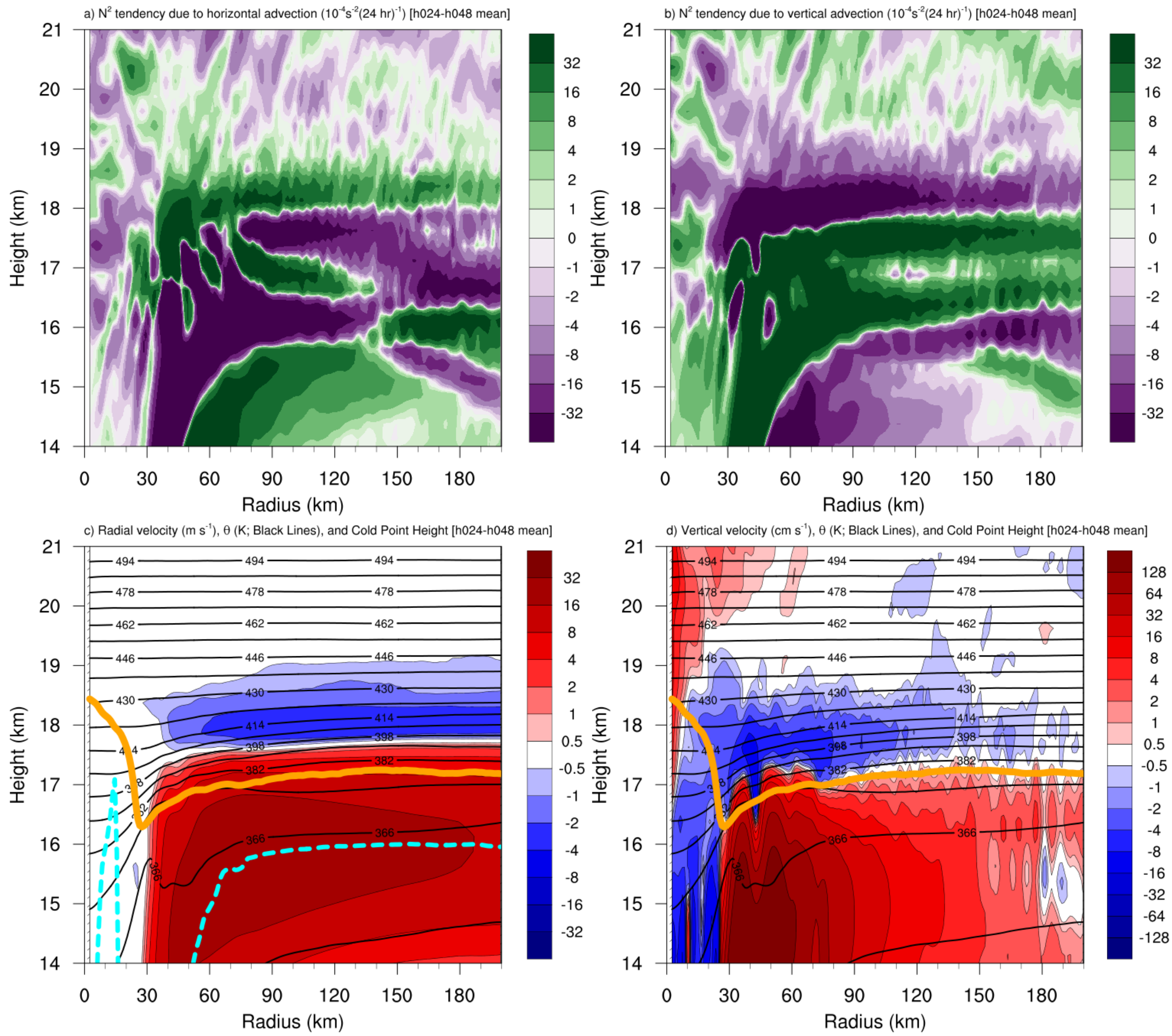

FIG. 8. The contribution to the change in N^2 over the 24-48-hour period (10^{-4} s^{-2} (24 hr)$^{-1}$) by (a) horizontal advection and (b) vertical advection. (c) The radial velocity (m s^{-1}; filled contours), potential temperature (K; thick black contours), cold-point tropopause height (orange line), and level of maximum outflow (dashed cyan line) averaged over the 24-48-hour period. (d) The vertical velocity (cm s^{-1}; filled contours), potential temperature (K; thick black contours), and cold-point tropopause height (orange line) averaged over the 24-48-hour period.

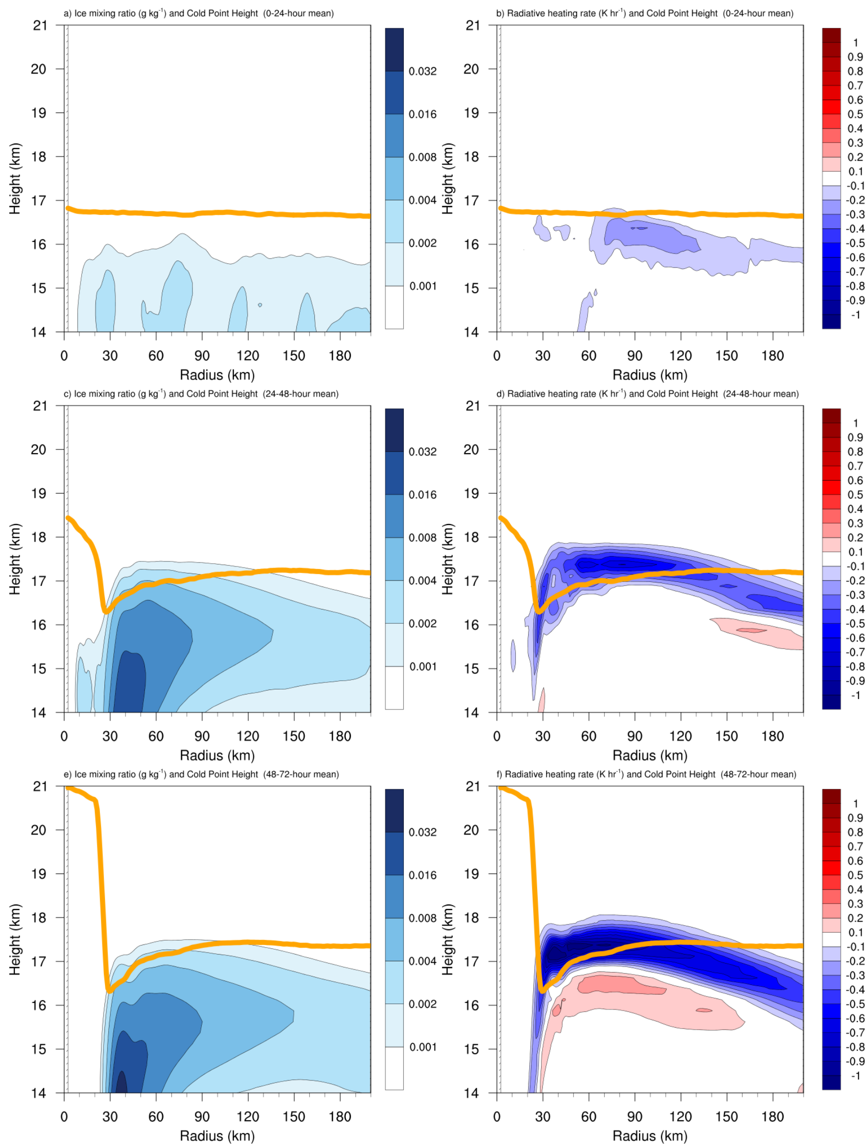

FIG. 9. Ice mixing ratio (g kg^{-1}) and cold-point tropopause height (orange lines) averaged over (a) 0-24 hours, (c) 24-48 hours, and (e) 48-72 hours. Radiative heating rate (K hr^{-1}) and cold-point tropopause height (orange lines) averaged over (b) 0-24 hours, (d) 24-48 hours, and (f) 48-72 hours.

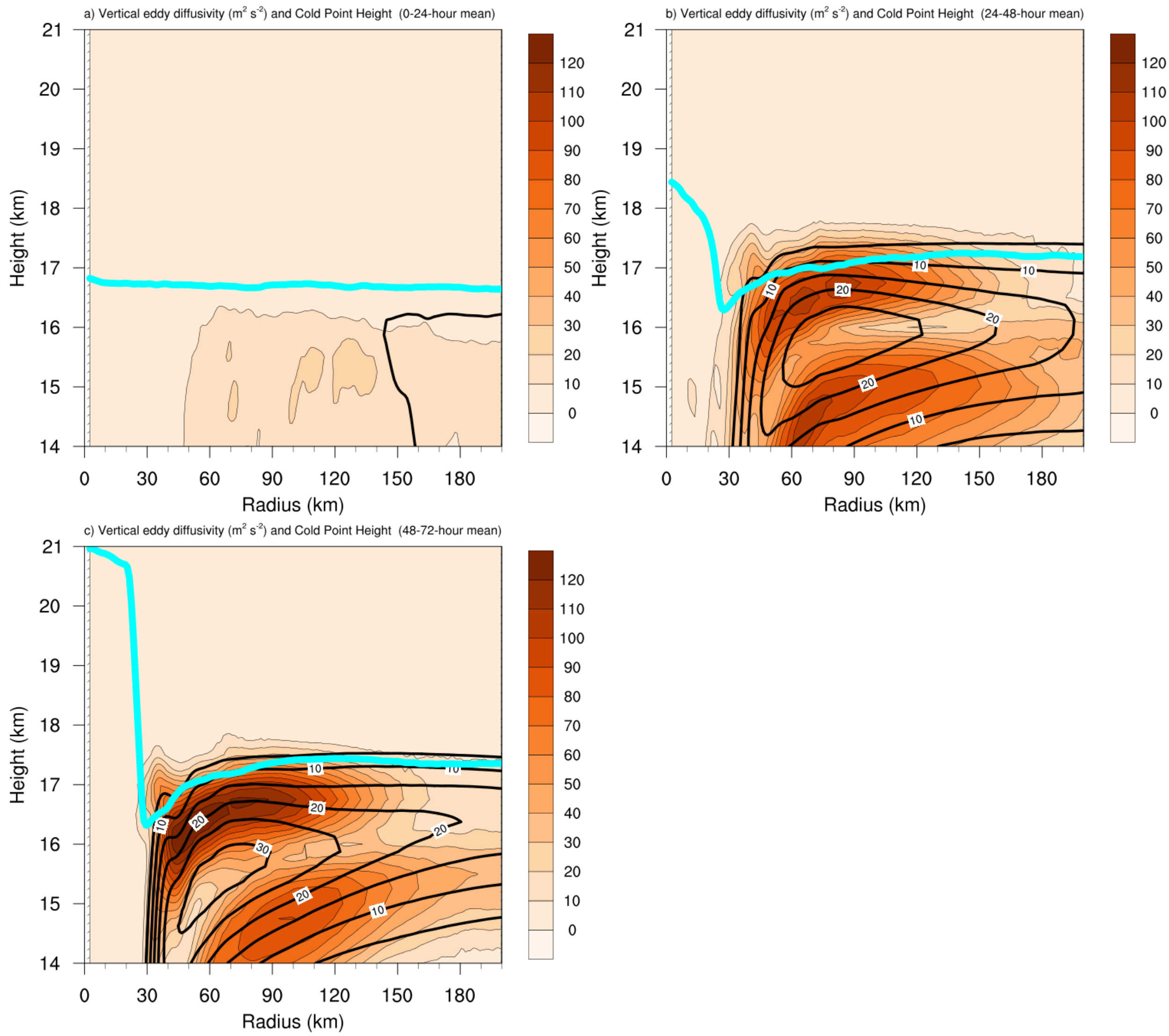

FIG. 10. Vertical eddy diffusivity (m^2 s^{-2}; filled contours), cold-point tropopause height (cyan lines), and radial velocity (m s^{-1}; thick black lines) averaged over (a) 0-24 hours, (b) 24-48 hours, and (c) 48-72 hours.